Journal of
Synchrotron Radiation

ISSN 0909-0495

Received 7 March 2008
Accepted 23 June 2008

Application of a pnCCD in X-ray diffraction: a three-dimensional X-ray detector

Wolfram Leitenberger,[a]* Robert Hartmann,[b,c] Ullrich Pietsch,[d] Robert Andritschke,[e,f] Ines Starke[g] and Lothar Strüder[e,f,d]

[a]Universität Potsdam, Institut für Physik, Germany, [b]MPI-Halbleiterlabor, München, Germany, [c]PNSensor GmbH, München, Germany, [d]Universität Siegen, FB Physik, Germany, [e]Max-Planck-Institut für extraterrestrische Physik (MPE), München, Germany, [f]MPI Halbleiterlabor, München, Germany, and [g]Universität Potsdam, Institut für Chemie, Germany.
E-mail: leitenberger@uni-potsdam.de

The first application of a pnCCD detector for X-ray scattering experiments using white synchrotron radiation at BESSY II is presented. A Cd arachidate multilayer was investigated in reflection geometry within the energy range 7 keV $< E <$ 35 keV. At fixed angle of incidence the two-dimensional diffraction pattern containing several multilayer Bragg peaks and respective diffuse-resonant Bragg sheets were observed. Since every pixel of the detector is able to determine the energy of every incoming photon with a resolution $\Delta E/E \simeq 10^{-2}$, a three-dimensional dataset is finally obtained. In order to achieve this energy resolution the detector was operated in the so-called single-photon-counting mode. A full dataset was evaluated taking into account all photons recorded within 10^5 detector frames at a readout rate of 200 Hz. By representing the data in reciprocal-space coordinates, it becomes obvious that this experiment with the pnCCD detector provides the same information as that obtained by combining a large number of monochromatic scattering experiments using conventional area detectors.

Keywords: pixel sensor; X-ray spectroscopy; pnCCD; GISAXS.

1. Introduction

pnCCD detectors were developed more than a decade ago (Strüder *et al.*, 2001). The most known application, but less known within the synchrotron community, is its use as a detector in X-ray telescope space missions, *i.e.* XMM-Newton, ABRIXAS and eROSITA (to be launched in 2010). As discussed below, a pnCCD has extraordinary properties for the detection of X-rays which makes it most attractive for the development of new experimental techniques in X-ray science.

The development of fast analytical X-ray methods is of major interest for the investigation of dynamic changes in the atomic and molecular structure of materials. Energy-dispersive X-ray methods are good candidates since they effectively use the entire available spectrum of a continuous X-ray source such as a synchrotron or X-ray tube, and energy discrimination is performed very fast electronically. Another important advantage is the possibility of a stationary experimental set-up during measurements in energy-dispersive mode. This fixed geometry provides fewer restrictions even to complicated, heavy and, at the same time, stable sample environments. In this context, energy-dispersive point detectors are already extensively and successfully used in many X-ray diffraction experiments (Giessen & Gordon, 1968; Nikulae *et al.*, 2006).

The aim of this paper is to present the first application of a pnCCD detector in an X-ray diffraction experiment with synchrotron radiation. This type of detector combines the advantages of a two-dimensional pixel detector with extremely fast readout with the good energy resolution of up-to-date solid-state X-ray detectors such as silicon drift detectors (Strüder, 2000). This means that every pixel of a pixel array can be used as an independent energy-dispersive detector. This type of detector can be called a 'colour camera for X-rays' (this is, of course, in another sense as the principle of colour cameras is for visible light working mostly with absorption filters). In our case the energy/colour of every X-ray photon is measured directly. Since we can already measure the position and energy of certain diffraction peaks in a stationary set-up, we can determine the intensity distribution in a certain volume of reciprocal space without performing any kind of scanning of the incidence or exit angle as it is known from various techniques of reciprocal space mapping *etc.* As a pnCCD can measure a three-dimensional dataset, it can be called a three-dimensional X-ray detector. The achievable

resolution in such a measurement is of course limited by the spatial resolution and the energy resolution of the detector and will be briefly discussed later.

At the moment there are other detector systems available which combine position sensitivity and energy resolution: (*a*) direct X-ray conversion in conventional MOS-CCDs, (*b*) scintillators coupled to optical MOS-CCDs (Tate *et al.*, 1997), (*c*) hybrid pixel detectors [*e.g.* PILATUS project (Broennimann *et al.*, 2006), MEDIPIX project (Llopart *et al.*, 2002)] and (*d*) the so-called active pixel sensors based on CMOS technology (Turchetta *et al.*, 2001, 2007). A collection of recent detector developments appeared in a special issue of this journal [*J. Synchrotron Rad.* (2006). **13**, 97–255]. The challenge for the use of position-, energy- and time-resolving detectors at synchrotron experiments is the simultaneous fulfillment of high detection efficiency, high frame rates (up to 1000 frame s^{-1}) to cope with the high photon flux, high radiation hardness to withstand the broadband bright X-rays without changes of detector performance, and low electronic noise to perform energy-resolved measurements in single-photon-counting mode. A few of the above-mentioned detectors combine some of the required properties, but never all of them. Conventional MOS-CCDs suffer from insufficient depletion depth, lack of readout speed and radiation tolerance (Strüder, 2000). The existing hybrid pixel detectors are designed and operated as photon counters. They fulfil all requirements except energy resolution. The CMOS sensors have not yet shown their performance in spectroscopy and their acceptable sensitivity to X-rays at higher energies in spectroscopic mode. The detector which comes closest to the above experimental wish list is the pnCCD: on 500 µm depleted silicon the quantum efficiency at 20 keV is still close to 40%, for a readout speed of up to 60 Mpixels s^{-1} the read noise is still below 3 electrons (r.m.s.) and, in addition, the devices have proven their radiation hardness in various experiments. The charge-handling capacity per pixel and per frame is of the order of 200000 electrons, *i.e.* corresponding to 100 X-rays of energy 8 keV.

Since this type of detector has been applied to an X-ray diffraction experiment for the first time, a brief description of the detector development and some basic technical properties are given. We shortly discuss the modes of data acquisition, distinguishing between single-photon-counting mode (SPC mode) and intensity mode (IM). In the second part of the paper we describe a first X-ray diffraction experiment carried out using white synchrotron radiation at the EDR beamline of BESSY in Berlin, Germany. Using a reflectivitiy-GISAXS (grazing-incidence small-angle X-ray scattering) experiment we have investigated an organic multilayer providing specular and off-specular scattering data for a wide range of energies simultaneously.

2. The pnCCD

The concept of the frame-store pn-junction charge-coupled device (FS pnCCD) is based on the pnCCD (Strüder, 2000) as developed for the X-ray satellite mission XMM-Newton (Strüder *et al.*, 2001). The device, of size 256 × 256 sensitive pixels with 75 µm × 75 µm pixel size, is fully depleted by reverse-biased voltages applied to pn-junctions on the front and back of the CCD. By the choice of appropriate voltage values, a potential minimum for electrons is created in the n-type silicon with an absolute minimum for electrons in a depth of about 8 µm. Incoming X-rays enter the image area of the CCD from the back (back-illuminated CCD) through the unstructured thin p-implanted layer, called back contact. The electron–hole pairs, generated by the X-ray photons, are separated owing to the applied electric field. The electrons drift to their potential minimum which is located inside a layer of low resistance (Fig. 1*a*). During photon integration time the signals are stored in the potential wells of the pixels built up by three transfer registers with two different voltage levels applied (three-phase CCD). Upon command the signals are transferred at high speed from the image to the frame store section that is usually shielded against X-rays (Fig. 1). The frame store comprises the same number of pixels as the image section but of smaller geometry. While new X-ray photons are accumulated in the image area for the subsequent picture, the previous image in the frame store is read out row by row.

The readout anode of each channel of the CCD is connected to the gate of a JFET, called 'first FET', which is monolithically integrated on the CCD chip (on-chip electronics). Wire bonds connect the source of this JFET of each channel with a dedicated analog amplifier array (CAMEX), being responsible for signal shaping and amplification, gain selection, signal processing and multiplexing (typically 128:1) and line driving. The output, *i.e.* 128 channels, is then transferred at typically 10 MHz per CAMEX output node to a fast ADC with 14-bit resolution. Presently, up to 10^3 frames s^{-1} can be read in the fastest configuration. The digitized data are transferred to a PC through an optical 1 GHz link. The front-end of a pnCCD system can be seen in Figs. 1(*c*) and 1(*d*).

The pnCCD system runs on a Linux-based platform. Data reduction can be performed with the help of an FPGA located on the ADC motherboard. Gain correction, offset correction, common mode rejection *etc.* are performed immediately after digitization. The final data analysis is carried out offline by the user depending on the type of experiment. A detailed description of the detector system can be found elsewhere (Hartmann *et al.*, 2006).

The main property of the pnCCD used for the present application is its capability to determine the energy of all photons absorbed in the active detector area by exactly analysing the amount of generated electrons in every pixel.

Every pixel acts as an individual energy-dispersive point detector operating at a sampling frequency equal to the frame rate. This so-called single-photon-counting mode requires an incoming photon flux which is on average less then 1 photon $pixel^{-1}$ within one readout cycle. The maximum number of correctly recordable photons per readout is much less than the number of pixels of the detector for several reasons. A single high-energy photon generates a large amount of electron–hole pairs in the active detector volume. From the activation energy of 3.6 eV for an electron–hole pair in silicon one obtains

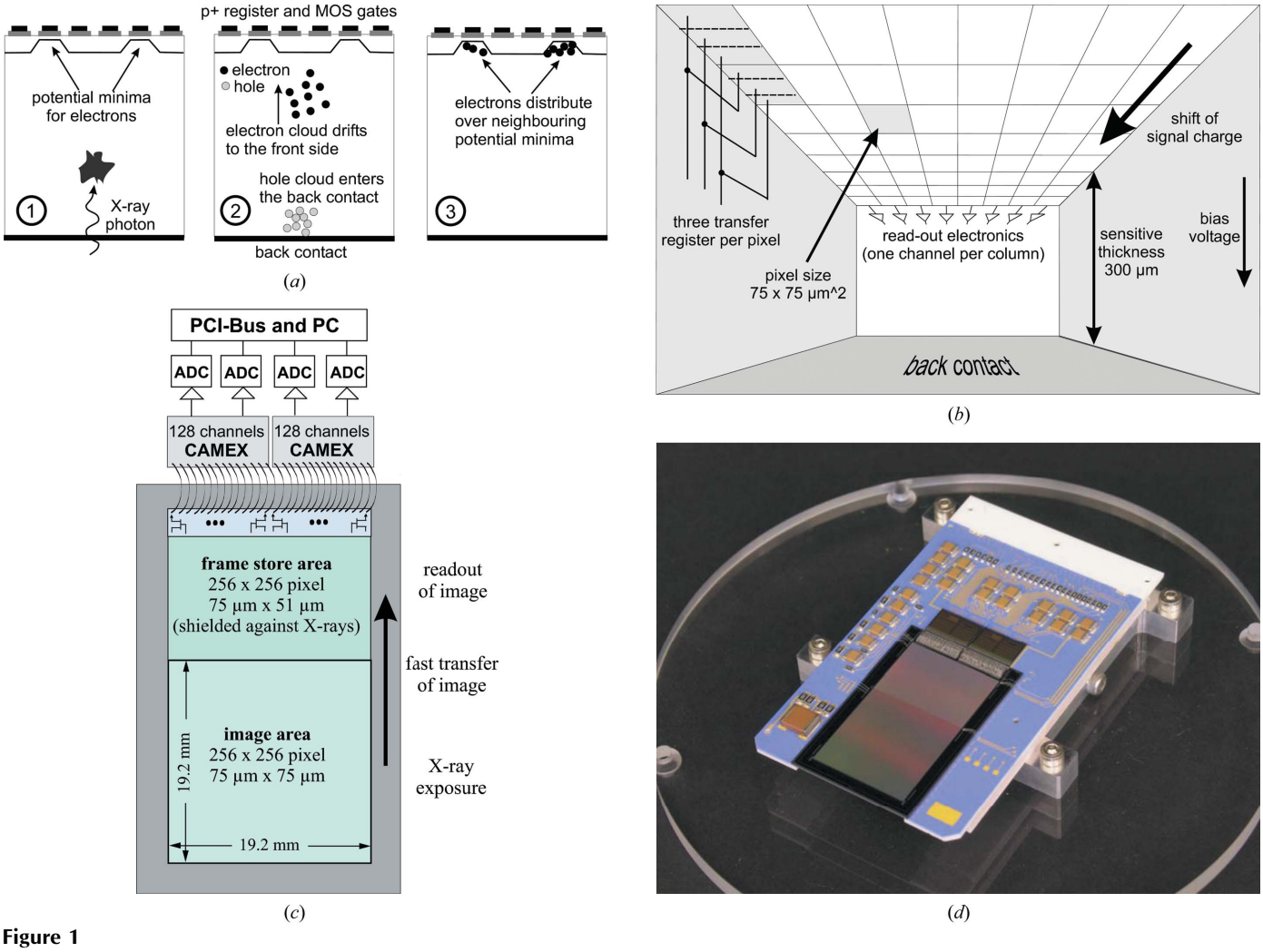

Figure 1
(*a*) Three stages of charge collection in a pnCCD. (1) Generation of charges inside the depleted bulk by irradiation. (2) Separation of charges by electric field. (3) Collection of charges in potential minima near the front contact and later on transfer to readout nodes. (*b*) Schematic view inside the fully depleted volume of the pnCCD. (*c*) and (*d*) pnCCD system of a 256 × 256 frame-store pnCCD, comprising a ceramic board with filter units and temperature control. The larger lower part of the pnCCD is the image area (75 µm × 75 µm pixels), the upper smaller part is the frame store area (51 µm × 75 µm pixels). The two CAMEX chips are wire bonded to the on-chip JFET of the pnCCD.

already 2778 e^- per 10 keV photon and the electrons generated by a single event are smeared in a charge cloud of diameter up to 100 µm and more depending on photon energy (Lutz, 2007). For that reason there is a large probability that electrons of a single event are collected in neighbouring pixels of the detector matrix (multi-pixel event). In this case the photon energy has to be determined from the sum of the charges collected in the connected pixels. The exact photon position is also at the centre of gravity of the illuminated pixels. The probability of three and four pixel events is estimated to be already much more than 50%.

In order to separate 'valid' from 'non-valid' events one has also to consider the spatial arrangement of coincidently illuminated pixels. For evaluation we considered up to four illuminated pixels per event but only in arrangements shown in Fig. 2. Furthermore, a direct neighbourhood of two or more events or even a jointly illuminated pixel makes the correct interpretation of the generating photon impossible. The same is true for events found in boundary pixels. However, all events should be separated from each other by at least one empty pixel in every direction. In this pixel a certain threshold level of about ten electrons should not be exceeded. In addition, one has to prevent so-called pile-up events. In case of one dominating photon energy in the spectrum there is a high probability that two photons of the same energy are recorded within one readout cycle and are interpreted as a single photon of twofold energy. For more details on the exact determination of a multi-pixel event, see Kimmel *et al.* (2006).

From the above discussion it becomes clear that a proper setting of the incoming photon flux is essential for successful experiments. In the case of strongly inhomogeneous illumination or even by the appearance of some 'hot spots' in the image, some pixels are illuminated near the limits whereas most of the pixels remain almost unexposed. In the overexposed detector regions the correct energy resolution is completely lost. For such cases one needs to adapt the experimental conditions by suited readout modes or shielding of highly illuminated detector regions.

Taking into account all these effects the maximum integral count rate at present hardware settings is of the order of a few thousand events per frame (roughly 1/40 of the pixel number in one frame). For the present experiment with a readout speed of about 200 Hz the typical total count rate was of the order of 10^5 to 10^6 events per second.

The maximum total count rate on the detector can be achieved when working in intensity mode. Here multiple photons can illuminate a pixel in a single readout cycle. Of course the energy information about the photons is completely lost. A single pixel can store in total about 2×10^5 electrons, which results in a maximum photon flux of about 70 photons of 10 keV per single pixel and frame. At 200 Hz readout speed this gives a maximum count rate of up to 10^7 photons s^{-1} cm^{-2} at this particular photon energy. This mode, however, was not further considered for the present experiment.

For the present experiment the detector chip, including part of the electronics, was installed inside a vacuum tank at pressure 10^{-6} mbar. The X-rays entered the vacuum chamber through a 125 µm-thick Kapton foil. The detector chip was cooled to 223 K in order to keep the noise level low. A thin aluminium coating protected the sensitive detector area from visible light exposure. The frame store region was additionally shielded against X-ray exposure by a 1 mm-thick copper plate. The detector could be aligned with respect to the beam by remote-controlled translation stages.

3. Advantage of a pnCCD for white-beam X-ray scattering experiments

In order to test the SPC mode we performed a reflectivity experiment at the white-beam EDR beamline at BESSY II. A short description of the beamline and a discussion about the equivalence of angular-dispersive and energy-dispersive reflectometry and diffraction can be found by Neissendorfer *et al.* (1999) and Pietsch *et al.* (2001). Located at a bending magnet, the distance between source and sample was about 30 m, and no optical elements, except slits and vacuum windows, are placed in the beam path between the source and the sample.

Owing to the critical energy of BESSY II of approximately 1 keV and the strong absorption of low-energy X-rays in air, the incident-beam spectrum appears as a glow-like curve with an onset energy of about 5 keV and an exponential decay in intensity at high energies. In total the incident-beam spectrum provides intensity between 5 keV and about 35 keV with an integrated flux of about 10^{10} photons s^{-1} into an area of 0.2 mm × 1 mm measured through an air pass of about 1 m. This total incident intensity can be further reduced by aluminium absorber foils of various thicknesses. The principal experimental set-up is shown Fig. 2.

The incident beam with wavevector k_i strikes the sample surface at an incident angle α_i and is reflected with an out-of-plane momentum k_f defined by the out-of-plane angle α_f and an in-plane angle φ. Using these three angles and the energy,

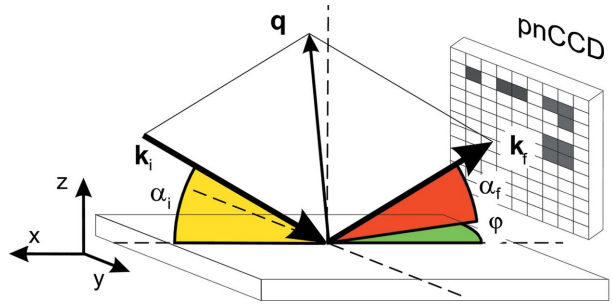

Figure 2
Definition of k_i, k_f and q and the relevant angles in the reflectometry experiment. In the CCD array the types of single- and multi-pixel events which were considered for evaluation are schematically shown in grey.

one can transform the experimental coordinates from angular into reciprocal space by

$$\begin{aligned} q_x &= k(\cos\alpha_f \cos\varphi - \cos\alpha_i), \\ q_y &= k \cos\alpha_f \sin\varphi, \\ q_z &= k(\sin\alpha_f + \sin\alpha_i), \end{aligned} \tag{1}$$

using $k = 2\pi/\lambda = 2\pi E/hc \simeq 0.507\,E[\mathrm{keV}]\,\text{Å}^{-1}$. Because α_i is a small angle and the other angles are also small owing to the small detector area, it yields

$$\begin{aligned} q_x &\simeq \tfrac{1}{2}kE\left(\alpha_i^2 - \alpha_f^2\right) + \alpha_f^2\left(\tfrac{1}{2}\varphi^2 - 1\right), \\ q_y &\simeq kE\varphi\left(1 - \tfrac{1}{2}\alpha_f^2\right), \\ q_z &\simeq kE(\alpha_f + \alpha_i). \end{aligned} \tag{2}$$

Considering the angular divergences and energy resolution of the detector, the resolution in q-space can be expressed by (Pietsch *et al.*, 2005)

$$\begin{aligned} \Delta q_x &= k\left[\Delta\alpha_f^2\alpha_f^2 + \Delta\alpha_i^2\alpha_i^2 + (\Delta E/2E)^2\left(\alpha_f^2 - \alpha_i^2\right)^2\right]^{1/2}, \\ \Delta q_y &= k\left[\Delta\varphi^2 + (\Delta E/E)^2\varphi^2\right]^{1/2}, \\ \Delta q_z &= k\left[\Delta\alpha_f^2 + \Delta\alpha_i^2 + (\Delta E/E)^2(\alpha_i + \alpha_f)^2\right]^{1/2}. \end{aligned} \tag{3}$$

We have measured a multilayer film of Cd arachidate as a test structure. The material is well investigated and consists of thin Cd^{2+} layers separated by a double layer made of $CH_3(CH_2)_{18}COO^-$ amphiphilic molecules (Geue *et al.*, 1999). Each double layer has a vertical lattice spacing of $d =$ 5.4 nm which provides a set of multilayer Bragg peaks whenever $\Delta q_z = 2\pi/d$ is fulfilled (see Fig. 3). In total, the film is stacked by nominally 10.5 bi-layers. This gives rise to Kiessig oscillations measuring the total film thickness D. Whereas the Bragg peaks are located along the q_z axis only ($q_x = q_y = 0$), the appearance of correlated interface roughness gives rise to diffuse scattering which is concentrated in sheets within the q_xq_y plane at $q_z = n2\pi/d$, where n is an ordinary number. In conventional experiments using monochromatic radiation both the multilayer Bragg peaks and correlated diffuse scattering are measured by so-called reciprocal space maps (Stömmer & Pietsch, 1996; Müller-Buschbaum & Stamm, 1998). This typically requires several scans such as detector scans (α_f varies for fixed α_i) and provides an intensity map within the q_zq_x plane. Another option is to run GISAXS scans

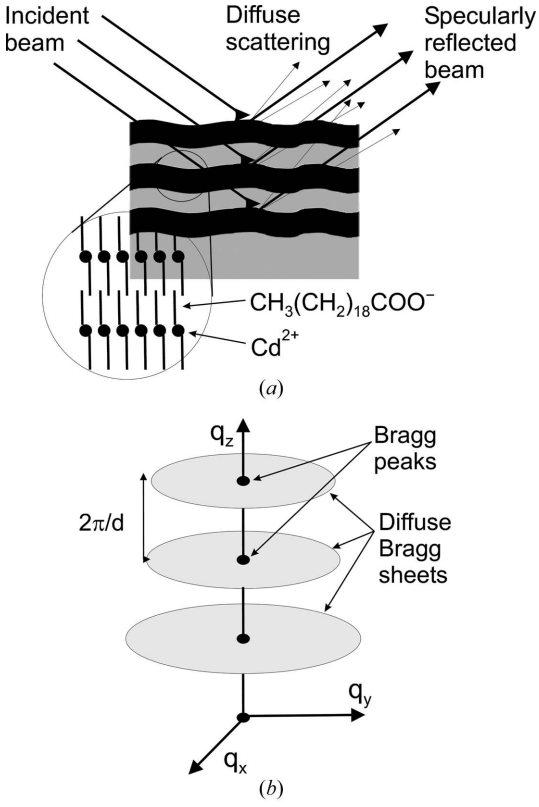

Figure 3
Schematic sketch of a Cd arachidate multilayer film (*a*) and its representation in reciprocal space (*b*).

(q_zq_y plane) using a two-dimensional detector at one fixed energy (Müller-Buschbaum, 2008).

Fig. 4 schematically shows several Ewald constructions for stationary diffraction experiments with a white or monochromatic incident-wavelength spectrum. The Ewald sphere is constructed in reciprocal space with a radius $|k| = 2\pi/\lambda$ and the k-vector of the incident beam is centred at the origin. Bragg diffraction occurs if the wavevector of the scattered photon $k_{h,x}$ ends at a reciprocal lattice point. A multiwavelength experiment (energy-dispersive mode) can be represented by several Ewald spheres with radii $|k_{0,\min}| < |k_{0,n}| < |k_{0,\max}|$ all centred along the incident-beam direction. For a certain direction of the scattered photons given by the angle 2θ (detector position) the scattered intensity is sampled along a straight line in reciprocal space ranging between $k_{h,\min}$ and $k_{h,\max}$.

The situation using an energy-dispersive point detector is shown in Fig. 4(*a*). Depending on the setting of α_i and α_f, one obtains a one-dimensional intensity distribution of a straight line through reciprocal space. For $\alpha_i = \alpha_f$ (specular scattering) this line contains the multilayer Bragg peaks; all other geometrical settings are oblique with respect to q_z and measure the diffuse scattering. Fig. 4(*b*) shows the situation for a monochromatic experiment using a one-dimensional line detector. Here the detector has access to several exit angles $2\theta_B$ and several k_h may hit the Ewald sphere simultaneously. This measures the specular scattering for a certain q_z and the diffuse scattering in its neighbourhood corresponding to a

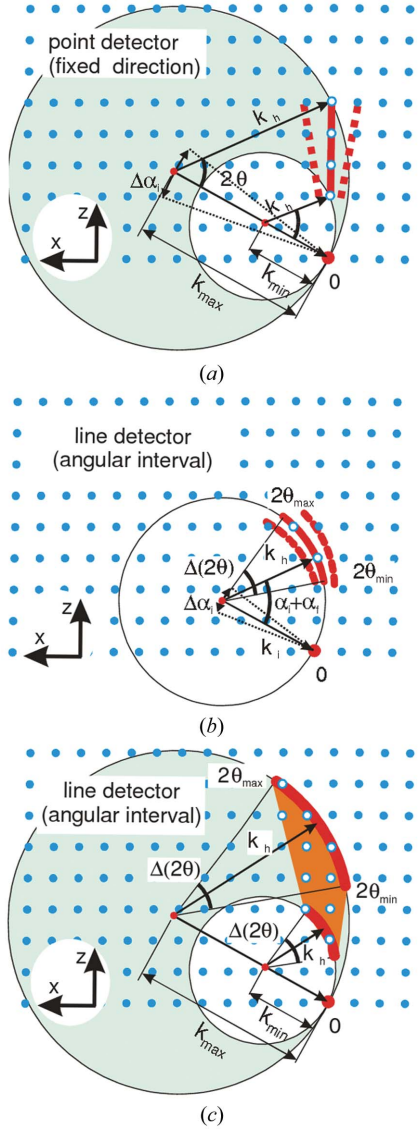

Figure 4
Three Ewald constructions show three different diffraction experiments in the q_xq_z plane of reciprocal space and illustrate (in red) the part of the reciprocal space which can be recorded by a static set-up. (*a*) White-beam incident spectrum with $\lambda_{min} < \lambda < \lambda_{max}$ and energy-dispersive point detector at fixed scattering angle 2θ. Scan along a straight line in the q_xq_z plane of reciprocal space. The dotted lines show the scan orientation for different incident beam directions (for that case no additional Ewald spheres are shown). (*b*) Monochromatic incident radiation with wavelength λ and a line detector measuring the angular region $2\theta_{min} < 2\theta < 2\theta_{max}$. Scan along a curved line in the q_xq_z plane of reciprocal space. The dotted lines show the orientation of the scan for different directions of the incident beam (for that case no Ewald spheres are shown). (*c*) White incident spectrum with $\lambda_{min} < \lambda < \lambda_{max}$ and energy-dispersive line detector measuring the angular region $2\theta_{min} < 2\theta < 2\theta_{max}$. Simultaneous scan of an area in the q_xq_z plane of reciprocal space between the two limiting Ewald spheres.

certain region in reciprocal space. A two-dimensional area detector extends the accessible q-space into the q_y direction and allows a two-dimensional area map in reciprocal space to be measured. Consequently the combination of a line detector where each pixel acts as an independent energy-dispersive detector combines the situation, shown in Figs. 4(*a*) and 4(*b*).

From Fig. 4(*c*) it becomes clear that an energy-dispersive line detector scans an area in q-space in between the two segments of the limiting Ewald spheres (red area). Subsequently a two-dimensional energy-dispersive detector (not shown) records a certain volume element Δq_x, Δq_y, Δq_z in reciprocal space and acts as a three-dimensional detector for an X-ray diffraction experiment.

4. X-ray reflectometry experiment with the pnCCD

To investigate the scattered intensity in a large q-space interval we realised two different experimental settings. The first was for high q-resolution near the specular beam and the second was for poor q-resolution but a large q-interval by measuring at larger scattering angles (see Fig. 5).

In the first setting the sample was illuminated by an incident white beam of size 2 mm × 0.1 mm (horizontal × vertical) at an incidence angle $\alpha_i = 0.8^\circ$. The detector was placed at a distance $L = 98$ cm from the sample and the detector was illuminated by the highly intense specularly reflected beam (detector on-axis). Since the intensity measured at the detector was too high to ensure the SPC mode, it was necessary to keep additional 2 mm aluminium foils as absorbers in the beam. In the second setting the detector was much closer to the sample ($L = 38$ cm) and was shifted by 2 mm out of the specularly reflected beam (detector off-axis) which resulted in a much lower and rather uniformly distributed scattering intensity. Using fewer extra absorbers we obtained again a photon flux well suited for working in SPC mode.

Each single dataset consists of all valid events extracted from 50000 to 100000 frames in total recorded with a readout speed of approximately 200 Hz, thus resulting in measurement times between 4 and 8 min. Integrated over the entire detector area the total number of events was 5×10^5 for the 'on-axis' experiment and 13×10^6 for the 'off-axis' experiment.

Because several detector components contain copper and iron, the recorded spectra always show a small amount of the fluorescence radiation created from those elements. The energy positions of these lines could be used for energy calibration. The spectral resolution of the detector was determined to $\Delta E = 150$ eV obtained from the full width at half-maximum (FWHM) of the copper $K\alpha$ line. This energy resolution is the same as that known from other energy-dispersive detectors such as silicon drift-detectors (Röntec) or Si(Li) detectors.

Fig. 6(*a*) shows the three-dimensional dataset obtained for the detector in the 'on-axis' position. The box surface shows the different projection of the measured three-dimensional intensity distribution. In order to explain the information contained in the figure, we present the data in energy space, *i.e.* $I(\alpha_f, \varphi, E)$ or equivalent $I(z, y, E)$ (Fig. 6*a*) and in reciprocal space $I(q_x, q_y, q_z)$ (Fig. 6*b*). In angular space the front plane

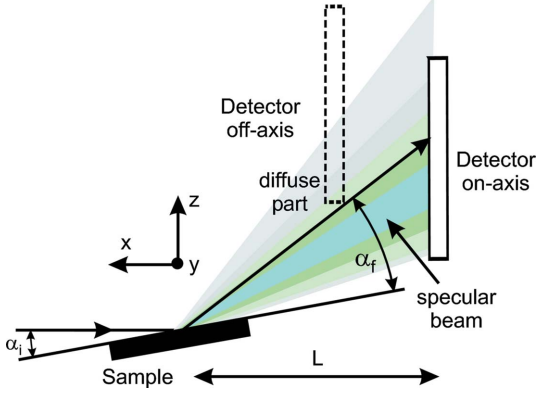

Figure 5
Set-up of the X-ray reflectometry experiment.

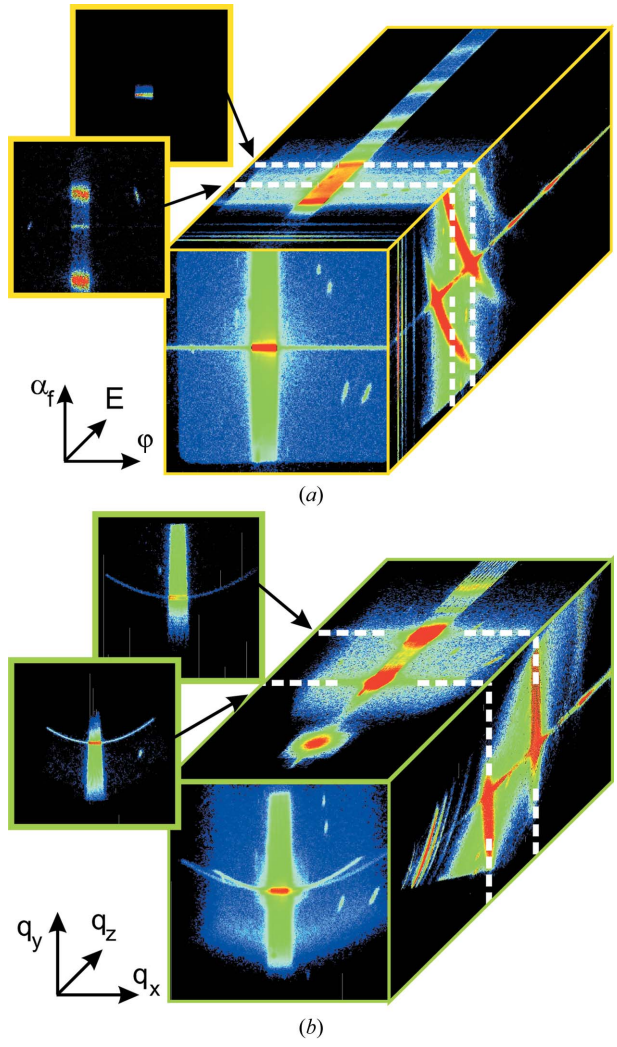

Figure 6
(*a*) Presentation of the three-dimensional dataset $I(z = \alpha_f, y = \varphi, E)$ recorded with the pnCCD in on-axis setting. For better visualization the measured intensity distribution is projected perpendicularly onto each of the three visible interfaces of the 'data-volume' limited by $-0.52^\circ < \alpha_f < 0.58^\circ$ in the z-axis, $-0.48^\circ < \varphi < 0.62^\circ$ in the x-axis, and 6 keV $< E <$ 35 keV. In addition, two slices of constant energy $E_1 = 20$ keV and $E_2 = 23$ keV are shown as insets providing similar information as a GISAXS experiment at this selected energy. (*b*) The data volume shown in (*a*) after transformation into reciprocal space $I(q_x, q_y, q_z)$. The data volume is limited by $-0.0015 < q_x < 0.0015$, $-0.12 < q_y < 0.12$, $0.0 < q_z < 0.5$ (all values in Å^{-1}). Insets: slices for constant q_z at the second- and third-order Bragg peak $q_z = 0.23$ Å^{-1} and $q_z = 0.34$ Å^{-1} (logarithmic colour scale).

corresponds to the spatial dimension of the active detector area which is 19 mm × 19 mm. The angular resolution in the xy plane for $L = 0.98$ m and a pixel size of 75 µm × 75 µm is $\Delta\alpha_f = \Delta\varphi = 0.76$ mrad.

The specular reflected beam of 2 mm × 0.1 mm (horizontal × vertical) is seen as the small horizontal stripe in the middle of the yz plane (front plane). The vertical band is caused by the diffusely scattered intensity summed up over all energies. The weak horizontal line is caused by a readout artifact owing to high intensity at the specular beam position.

The third dimension of the image, the photon energy, is displayed in the range 6 keV < E < 55 keV. This interval is divided into 512 intervals of ∼100 eV energy width. All together this results in a three-dimensional dataset containing 512 GISAXS images. The images for any single selected energy (see inset) may contain one or more maxima. The top plane represents the sum over the yE plane of the dataset. It contains several multilayer Bragg peaks at energies fulfilling the Bragg condition [equation (1)]. The width in the y-direction is given by the horizontal beam extension. Finally the side plane of the box is the zE plane containing the multilayer Bragg peaks and the sheets of diffuse scattering of the multilayer. In energy space these diffuse sheets are curved. By chance we have observed additional diffraction spots of small size. These spots look like Bragg peaks but the origin of this scattering could not be identified. Nevertheless, the appearance of these spots demonstrates the capability of the detector to identify sharp scattering events in three-dimensional data space.

Clearer information is obtained after transformation of the data into reciprocal space using equation (1) (Fig. 6*b*). Here the front area of the three-dimensional data volume is spanned by q_x, q_y and the third dimension is q_z. It becomes clear that the diffuse sheets are centred at the q_z positions of multilayer Bragg peaks and extended into the q_xq_y plane. On the other hand the Cu-fluorescence, which is seen as an almost homogeneously illuminated plane in the energy space figure, appears as a bent line in reciprocal space. The line artifact in the front plane is also bent now.

The limits of the displayed q-volume do not coincide exactly with the limits of the accessible q-space volume of the measurement. Some parts having low intensity were skipped in order to improve the overall image quality and to see more detail in the remaining q-space.

As seen from equation (3) and Fig. 6(*b*), the resolution element of each voxel in q-space is dependent on several parameters. It may change by more than an order of magnitude within small distances. The resolution values are in the range 10^{-5} Å^{-1} < Δq_x < 10^{-3} Å^{-1} and $\Delta q_z \simeq 2 \times 10^{-3}$ Å^{-1}. The resolution Δq_y is of the order of 10^{-2} Å^{-1} which is a much lower resolution than would be obtainable with the detector. In this case the horizontal beam width of 2 mm is the limiting factor. Since no structures of the diffraction pattern parallel to the layers were expected, we choose a homogeneous illumination in the horizontal plane.

Fig. 7(*a*) shows the spectral distribution of the photons recorded in both the specular beam region of size 4 × 30 pixels

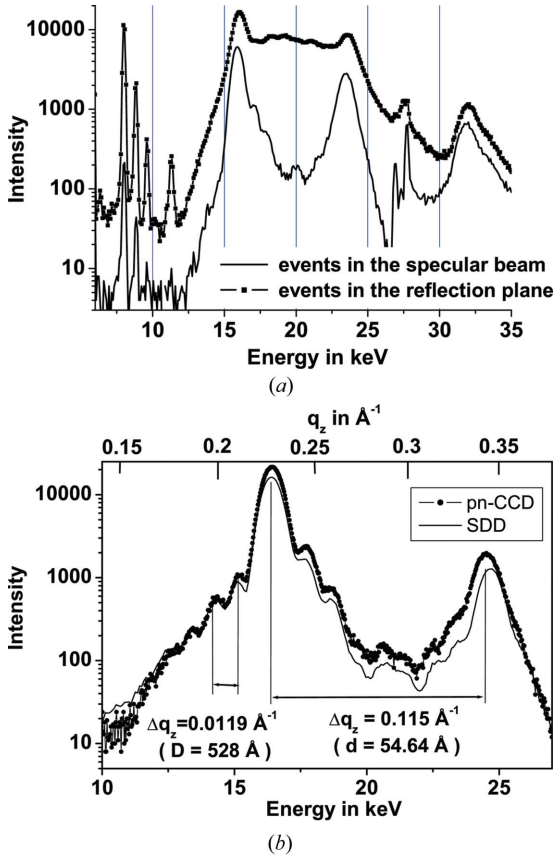

Figure 7
(*a*) Spectral distribution of all events recorded with the CCD in the specular beam region (line) and in the whole reflection plane (symbols) (in total 5×10^5 events are considered). (*b*) Comparison of energy spectra of the specular reflected beam measured with the pnCCD (symbols) and a Si drift diode detector (line).

(vertical × horizontal) and in the entire reflection plane of 256 × 30 pixels (vertical × horizontal) seen in the yz plane of Fig. 7(*a*). High-contrast and even Kiessig fringes are visible when looking at the specular beam region only. The intensity maxima at 16 keV and 24 keV are the second- and third-order multilayer Bragg peaks. Owing to absorption of the absorber foils the first-order Bragg peak is not registered. It would appear approximately at the energy where the $K\alpha$ and $K\beta$ lines of copper are registered. Based on the two multilayer Bragg peaks which were recorded, the lattice spacing of the multilayer is determined by $d_{ML} = 2\pi/\Delta q_z$ using $q_z \simeq \alpha_1 E$ (here q is given in Å^{-1} and E in keV). With $\Delta q_z = 0.115$ Å^{-1} we obtain $d_{ML} = 2\pi/\Delta q_z = 54.64$ Å. From Kiessig fringes one obtains a total layer thickness of $D = 528$ Å. In Fig. 7(*b*) an energy spectrum extracted from pnCCD measurements is compared with an energy spectrum measured with an energy-dispersive point detector [silicon drift detector (SSD) Xflash, Roentec] taken under the same experimental conditions. Both spectra agree well with each other even in their details.

In order to record a larger angular interval of the diffusely scattered intensity we measured the scattering again in off-axis setting realised by a sample-to-detector distance $L = 38$ cm and an angle of incidence $\alpha_i = 2.0°$. The detector was moved upwards so that the specular beam was 1 mm below the lower

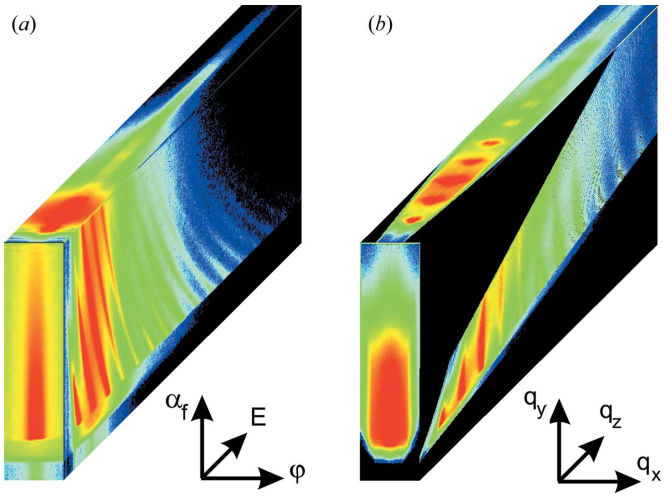

Figure 8
Presentation of a three-dimensional dataset of diffuse scattering of a Cd arachidate multilayer film in the same projection view and same orientation as in Fig. 6. (*a*) Energy space, and (*b*) reciprocal space. The limits of the q-space volume are $-0.03 < q_x < 0$, $-0.03 < q_y < 0.03$ and $0.2 < q_z < 1.5$ (all values in Å^{-1}).

edge of the detector. In this arrangement we could observe the diffuse scattering in the reflection plane above the specular beam within an interval $0.5° < \Delta\alpha_f < 3.0°$. A few pixel rows at the bottom of the CCD were shadowed by metal shielding and so the smallest accessible angular value was $\Delta\alpha_f = 0.6°$. Since the highly intense specular beam was not hitting the detector we could remove all the extra absorbers and extend the recorded energy spectrum to smaller values still ensuring operation in SPC mode.

To further increase the readout rate we selected an area of interest of 64 × 256 pixels (horizontal × vertical) within the detector area and read out these pixels only. The readout speed could be increased to 275 frames s^{-1}. The dataset after collection of 50 frames contained 1.3×10^7 valid events corresponding to an average of 260 events per frame.

The width of the incident beam was again 2.0 mm × 0.1 mm (horizontal × vertical). We evaluated the measured data as with the first dataset. Since the horizontal width of the incoming beam was 2 mm, the angular resolution of angle φ was again very poor. However, the recorded data can be presented in a similar way as in the first experiment. Fig. 8 shows the scattered intensity in energy space and in reciprocal space. As for the first dataset the limits of the displayed q-space volume do not coincide with the limits of the measured q-space volume.

Both graphs clearly show several sheets of diffuse resonant scattering. They are bent in energy space (Fig. 8*a*) but parallel to q_x and q_y in reciprocal space (Fig. 8*b*). However, the measured intensity distributions shown in this paper are not corrected or normalized to the intensity distribution of the incident spectrum $I_0(E)$ of the white beam. A more quantitative evaluation would require an individual correction to that spectrum for every pixel.

Fig. 9 shows the combined reciprocal-space maps within the q_zq_x plane extracted from the three-dimensional datasets

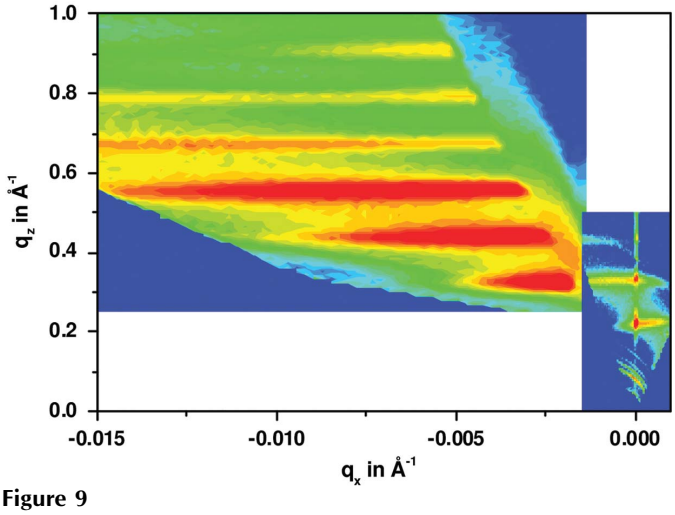

Figure 9
Combined contour plot of the specular and the off-specular measurement in the q_xq_z plane. The two regions in reciprocal space almost do not overlap (logarithmic colour table used).

shown in Figs. 6(*b*) and 8(*b*). The specular dataset on the lower right-hand side contains the specular beam with the equidistant Bragg peaks and a small part of the diffuse sheets. The off-specular dataset shows the diffuse sheets in a wide q_x range with lower resolution up to the eighth order owing to different experimental geometry. Note that the information seen in this mapping was recorded in only a few minutes. This has to be compared with the several hours required for recording data in angular-dispersive mode owing to the need to scan several angular parameters one after another. The data recorded in the second setting exclude the region close to $q_x = 0$ which is important for quantitative analysis.

It is well known that diffuse scattering of fatty acid salt multilayers, such as Cd arachidate, do not match the correlated roughness model introduced by Sinha *et al.* (1988). Stömmer & Pietsch (1996) showed that the particular roughness model can be determined by plotting the FWHM of diffuse sheets Δq_x as a function of q_z. This type of data evaluation seems to be possible using the present pnCCD data. A detailed analysis of the roughness model will be presented elsewhere.

5. Discussion and conclusion

In this paper we have shown the first application of a pnCCD for an X-ray diffraction experiment. Using white synchrotron radiation we measured a volume in reciprocal space using a fixed experimental set-up. Compared with a monochromatic experiment using a two-dimensional detector, the pnCCD unifies several GISAXS pictures taken at different X-ray energies. Finally the pnCCD combines 256 × 256 independent energy-dispersive detectors which is an advantage for white-beam experiments. This detector is well suited for performing time-dependent experiments, *i.e.* analyzing structural variation induced by an external perturbation. Owing to the fact that the experimental conditions (*i.e.* geometry) can be kept fixed during the experiment, there is no need for extra data

corrections except those which have to be made for all frames with the same formalism. One obtains three-dimensional information of the sample changing as a function of time.

The achievable time resolution in an experiment is determined by the readout time of the detector. The full frame readout was 5 ms in the present experiment. In SPC mode one needs to accumulate a minimum of about 10^4 frames in order to obtain sufficient counting statistics resulting in a real-time resolution of about 50 s. This can be improved by a factor up to 10^3 using an improved detector system allowing a faster readout time of 5 µs per frame, which is in preparation. Moreover, much faster readout times can be achieved if the readout area contains a reduced number of pixels, *e.g.* groups of several detector lines. Also, data reduction should be carried out before storing data.

Another limitation is given by the total number of photons which can be accepted in single-photon mode. Considering a homogeneous distribution of intensity among the $256^2 = 65536$ pixels, the total number on the detector is 1.3×10^7 photons s^{-1} within the whole energy range (taking 200 frames s^{-1}). This can be increased to several 10^9 photons s^{-1} in the case of 5 µs per frame readout. However, at this incoming photon number the detector has already lost its capability for energy resolution as mentioned before. However, for high count rate working in intensity mode the detector is a high-speed and low-noise black and white camera. This mode can be used for time-resolved experiments with monochromatic or pink beam with a time resolution down to 5 ms for full frame readout.

The strong dependence of the detector response on local intensity requires analysis of counting events of each pixel. As seen in Fig. 6, the so-called cross-talking events cannot be excluded in case the intensity at a particular pixel exceeds a certain level. As mentioned before, the analysis of the intensity distribution among neighbouring pixels is absolutely necessary in order to select a non-valid event. Furthermore, pile-up effects need correcting.

In conclusion, the pnCCD provides new possibilities for X-ray diffraction experiments or other experiments with hard X-rays. In our first experiments we have recorded a three-dimensional dataset using a stationary experimental set-up. At its present state of development the detector system has been operated at a photon flux that is available at laboratory X-ray sources. However, at present the high quantum efficiency over the large detector area, low noise and fast readout rate qualify the system for several types of position-resolved X-ray spectroscopy applications at moderate photon flux. After upgrading the system with respect to a much faster readout time, high-intensity adapted off-line analysis and a larger frame area, the detector system will unfold its full potential for experiments with much higher photon flux. Moreover, the application of the detector system requires a change in the experimental strategy compared with conventional photon counters or integrating detectors and it requires particular knowledge of the detection processes. Taking 65×10^3 pixels per frame at a readout speed of 200 Hz gives a total data volume of 26 Mbyte per second or already 2.6 Gbyte after 100 s of data collection. To be able to process that amount of data generated by the present system, or even much larger data volumes of faster systems, certain software routines have to be developed. They must allow a high-speed pre-selection of valid events and online data reduction in order to enable a fast pre-analysis of the measured data. Further on each type of experiment requires an optimized readout mode which has to be developed in order to make use of the full potential of the detector system. Software developments are on the way to allow operation of the very complex detector system in a convenient way. The pnCCD will be a useful detector for experimentalists in many fields of X-ray science.

This work was supported by BMBF Verbundforschung, project number 05KS7PSA. We gratefully acknowledge the financial support of the MPI für Kolloid und Grenzflächenforschung, Potsdam-Golm.

References

Broennimann, Ch., Eikenberry, E. F., Henrich, B., Horisberger, R., Huelsen, G., Pohl, E., Schmitt, B., Schulze-Briese, C., Suzuki, M., Tomizaki, T., Toyokawa, H. & Wagner, A. (2006). *J. Synchrotron Rad.* **13**, 120–130.

Geue, T., Schultz, M., Englisch, U., Stömmer, R., Pietsch, U., Meine, M. & Vollhardt, D. (1999). *J. Chem. Phys.* **110**, 8104–8111.

Giessen, B. L. & Gordon, G. E. (1968). *Science*, **159**, 973–975.

Hartmann, R., Buttler, W., Gorke, H., Herrmann, S., Holl, P., Meidinger, N., Soltau, H. & Strüder, L. (2006). *Nucl. Instrum. Methods Phys. Res. A*, **568**, 118–123.

Kimmel, N., Hiraga, J. S., Hartmann, R., Meidinger, N. & Strüder, L. (2006). *Nucl. Instrum. Methods Phys. Res. A*, **568**, 128–133.

Llopart, X., Campbell, M., Dinapoli, R., Segundo, D. S. & Pemigotti, E. (2002). *IEEE Trans. Nucl. Sci.* **49**, 2279–2283.

Lutz, G. (2007). *Semiconductor Radiation Detectors.* Berlin: Springer.

Müller-Buschbaum, P. (2008). *Polymer Surfaces and Interfaces: Characterization, Modification and Applications*, edited by M. Stamm. Berlin: Springer.

Müller-Buschbaum, P. & Stamm, M. (1998). *Macromolecules*, **31**, 3686.

Neissendorfer, F., Pietsch, U., Brezesinski, G. & Möhwald, H. (1999). *Meas. Sci. Technol.* **10**, 354–361.

Nikulae, P., Lechner, P., Soltau, H., Lutz, G., Strüder, L., Fiorini, C. & Longoni, A. (2006). *Nucl. Instrum. Methods Phys. Res. A*, **568**, 336–341.

Pietsch, U., Grenzer, J., Geue, T., Neissendorfer, F., Brezesinski, G., Symietz, C., Möhwald, H. & Gudat, W. (2001). *Nucl. Instrum. Methods Phys. Res. A*, **467–468**, 1077.

Pietsch, U., Holy, V. & Baumbach, T. (2005). *High-Resolution X-ray Scattering from Thin Films to Lateral Nanostructures.* Berlin: Springer.

Sinha, S. K., Sirota, E. B., Garoff, S. & Stanley, H. B. (1988). *Phys. Rev. B*, **38**, 2297–2311.

Stömmer, R. & Pietsch, U. (1996). *J. Phys. D*, **29**, 3161–3165.

Strüder, L. (2000). *Nucl. Instrum. Methods Phys. Res. A*, **454**, 73–113.

Strüder, L., Briel, U., Dennerl, K., Hartmann, R., Kendziorra, E., Meidinger, N., Pfeffermann, E., Reppin, C. & Aschenbach, B. (2001). *Astron. Astrophys.* **365**, L18–L26.

Tate, M. W., Gruner, S. M. & Eikenberry, E. F. (1997). *Rev. Sci. Instrum.* **68**, 47–54.

Turchetta, R., Berst, J., Casadei, B., Claus, G., Colledani, C., Dulinski, W., Hu, Y., Husson, D., Le Normand, J., Riester, J., Deptuch, G., Goerlach, U., Higueret, S. & Winter, M. (2001). *Nucl. Instrum. Methods Phys. Res. A*, **458**, 677–689.

Turchetta, R. *et al.* (2007). *Nucl. Instrum. Methods Phys. Res. A*, **582**, 866–870.